International Journal of Mass Spectrometry 308 (2011) 265–274

Contents lists available at ScienceDirect

International Journal of Mass Spectrometry

journal homepage: www.elsevier.com/locate/ijms

Collision-induced dissociation of MO^+ and MO_2^+ (M = Ta and W): Metal oxide and dioxide cation bond energies[☆]

Christopher S. Hinton[a], Murat Citir[a], Manuel Manard[b], P.B. Armentrout[a,*]

[a] Chemistry Department, University of Utah, 315 S. 1400 E. Rm 2020, Salt Lake City, UT 84112, United States
[b] National Security Technologies, LLC, Special Technologies Laboratory, 5520 Ekwill St., Santa Barbara, CA 93111, United States

ARTICLE INFO

Article history:
Received 17 May 2011
Received in revised form 14 June 2011
Accepted 16 June 2011
Available online 23 June 2011

Keywords:
Bond energies
Guided ion beam
Metal dioxides
Metal oxides
Tantalum
Tungsten

ABSTRACT

The collision-induced dissociation (CID) of TaO^+, WO^+, TaO_2^+, and WO_2^+ with Xe along with reactions of TaO^+ and WO^+ with O_2 are studied as a function of kinetic energy using guided ion beam tandem mass spectrometry in order to elucidate the thermochemistry of the MO_2^+ species. The kinetic energy dependences for the CID reactions show endothermic behavior, whereas the $MO^+ + O_2 \rightarrow MO_2^+ + O$ reactions proceed near the collision limit indicating exothermic processes. Analyses of the endothermic CID reaction cross sections yield 0 K threshold energies in eV of $E_0(Ta^+–O) = 7.01 \pm 0.12$, $E_0(W^+–O) = 6.72 \pm 0.10$, $E_0(OTa^+–O) = 6.08 \pm 0.12$, and $E_0(OW^+–O) = 5.49 \pm 0.09$. The nature of the bonding in MO^+ and MO_2^+ is discussed and compared for Ta and W and analyzed using theoretical calculations at the B3LYP/HW+/6-311+G(3df) level of theory. Bond energies for all MO^+ and MO_2^+ species are calculated using geometries calculated at this level as well as BHLYP and CCSD(T) levels and the Stuttgart–Dresden (SDD) and the Def2TZVPP basis sets. Reasonable agreement between the theoretical bond energies and experimental CID threshold energies for TaO^+, WO^+, TaO_2^+, and WO_2^+ is found. Potential energy surfaces for the reaction of the metal cations with O_2 are also calculated at the B3LYP level of theory and reveal additional information about the reaction mechanisms.

1. Introduction

The oxides of transition metals have properties that enable them to play vital roles in industrial, organometallic, and atmospheric chemistry [1–3]. In understanding the origins of these important properties, it can be useful to study the binding of the simplest examples of each species. Insight into the interaction of the metals and their oxides with O_2 can be obtained by examining reactions in the gas phase using a guided ion beam tandem mass spectrometer. The gas phase is an ideal arena for detailed study of the energetics of bond-making and bond-breaking processes at a molecular level. Because metal supports and interactions are absent, quantitative thermodynamic and intrinsic mechanistic information for various bond activation processes can be obtained.

Our group has previously used guided ion beam tandem mass spectrometry to study diatomic metal monoxide cations, MO^+, of the first-row [4–12], second-row [6,10,13–18], transition metals and other metals [10,19–21], but as yet have examined only a few third-row transition metals [22–24]. Likewise, our work has encompassed fewer studies of metal dioxide cations, MO_2^+, which include first-row [10,11], second-row [10,15–18], third-row [25] transition metals, and other metal cations [10]. In the present study, we extend these studies to the third-row transition metal ions, tantalum and tungsten. Using guided ion beam tandem mass spectrometry, we obtain the kinetic energy dependences of both exothermic and endothermic processes involving these species. Analyses of such data provide experimental thermochemistry that can be used as benchmarks for comparison with theoretical models of the structure of the metal oxides and dioxides.

Previous thermodynamic information on the monoxide and dioxide cations of tantalum and tungsten originates from several sources and is summarized in Table 1. In our laboratory, we have examined the endothermic reaction of Ta^+ with CO, yielding the bond dissociation energy (BDE) of $Ta^+–O$ as 7.10 ± 0.12 eV [23]. This value agrees nicely with 7.18 ± 0.14 as derived using Eq. (1)

$$D(M–O) + IE(M) = D(M^+–O) + IE(MO) \qquad (1)$$

and the values $IE(Ta) = 7.5495$ eV [26], $D_0(TaO) = 8.24 \pm 0.13$ eV from Pedley and Marshall [27], and $IE(TaO) = 8.61 \pm 0.02$ eV from a photoelectron experiment of Dyke et al. [28] (see [23] for further details). These values contrast with that listed in a review by Schröder et al. [29], $D(Ta^+–O) = 8.15 \pm 0.65$ eV, taken from information in the GIANT compilation [30], which uses older values for $IE(Ta) = 7.40$ eV [31] and $IE(TaO) = 7.92 \pm 0.1$ eV [32], along with $\Delta_f H_0(TaO) = 2.08 \pm 0.65$ eV [33], and also

---

[☆] In honor of John R. Eyler's many contributions to ion chemistry and spectroscopy.
[*] Corresponding author. Tel.: +1 801 581 7885; fax: +1 801 581 8433.
E-mail address: armentrout@chem.utah.edu (P.B. Armentrout).

1387-3806/$ – see front matter © 2011 Elsevier B.V. All rights reserved.
doi:10.1016/j.ijms.2011.06.011

Table 1
Experimental thermochemical data for tantalum and tungsten oxides and dioxides.

M^+–O	IE(M)	D_0(M–O)	IE(MO)	$D_0(M^+–O)$	
				Literature	This work
Ta^+–O	7.5495[a]	8.16 ± 0.12[b] 8.24 ± 0.13[c] 8.4 ± 0.5[d] 8.65 ± 0.65[e]	8.69 ± 0.18,[b] 8.61 ± 0.02[f] 7.92 ± 0.1,[g] 7.5 ± 0.5[h] 6 ± 0.5,[d] 8.70 ± 0.17[i]	7.10 ± 0.12[b] 7.18 ± 0.14[a,c,f] 8.15 ± 0.65[j]	7.01 ± 0.12
W^+–O	7.864[k]	7.01 ± 0.31[b] 6.92 ± 0.44[c] 6.95 ± 0.44[l]	8.04 ± 0.45,[b] 8.1 ± 0.3,[m] 9.1 ± 1,[n] 7.19 ± 0.32[i]	6.77 ± 0.07[b] 6.68 ± 0.53[c,k,m] 7.16 ± 0.43[m] 5.46 ± 0.43[j]	6.72 ± 0.10
OTa^+–O		6.87 ± 0.23[h] 6.61 ± 0.92[d,l]	8.5 ± 0.5,[h] 9 ± 0.5[d] 9.54 ± 0.32[i]	6.07 ± 1.05[j] 6.73 ± 0.80[d,f,h]	6.08 ± 0.12
OW^+–O		6.15 ± 0.53[l]	9.6 ± 0.3,[o] 9.5 ± 0.5,[p] 9.9 ± 1.0,[q] 9.8,[r] 9.9 ± 0.6[n] 8.76 ± 0.69[i]	5.72 ± 1.17[j] 4.6_5 ± 0.7[l,m,o]	5.49 ± 0.09

[a] Simard et al. [26].
[b] Armentrout et al. [23].
[c] Pedley and Marshall [27].
[d] Inghram et al. [37].
[e] Lias et al. (GIANT Tables) [30].
[f] Dyke et al. [28].
[g] Ackermann et al. [32].
[h] Smoes et al. [38].
[i] This work.
[j] Schröder et al. [29].
[k] Campbell-Miller and Simard [35].
[l] JANAF tables [33].
[m] Blagojevic et al. [34], corrected to 0 K.
[n] DeMaria et al. [36].
[o] Gusarov et al. [39].
[p] Balducci et al. [40].
[q] Yamdagni et al. [41].
[r] Drowart et al. [42].

leads to $D_0(TaO) = 8.65 \pm 0.65$ eV. Likewise, we have previously measured the W^+–O BDE as 6.77 ± 0.07 eV from the endothermic reaction of W^+ with CO [23]. Again this agrees well with $D_0(W^+–O) = 6.68 \pm 0.53$ eV calculated using Eq. (1) and $D_0(WO) = 6.92 \pm 0.44$ eV from Pedley and Marshall [27], IE(WO) = 8.1 ± 0.3 eV measured by Bohme and co-workers [34], along with IE(W) = 7.864 eV [35]. As for TaO^+, this value disagrees with that quoted by Schröder et al. [29] of $D(W^+–O) = 5.46 \pm 0.43$ eV derived from information in the GIANT compilation [30], which uses IE(W) = 7.60 eV [31], IE(WO) = 9.1 ± 1 eV [36], and $\Delta_f H_0(WO) = 4.41 \pm 0.43$ eV [33], and also leads to $D_0(WO) = 6.95 \pm 0.44$ eV. Bohme and co-workers [34] also determined that W^+ reacts with COS to form WO^+ at room temperature with an efficiency of 0.38. They took this to indicate that $D_{298}(W^+–O) > D_{298}(O–CS) = 6.85 \pm 0.04$ eV, which they combined with $D_{298}(W^+–O) = 6.81 \pm 0.82$ eV to yield a refined range of values that they cited as $D_{298}(W^+–O) = 7.20 \pm 0.43$ eV. This value can be adjusted to $D_0(W^+–O) = 7.16 \pm 0.43$ eV, Table 1.

Literature information on the dioxides of Ta^+ and W^+ is less plentiful. Bond energies and ionization energies of the metal monoxides and dioxides can be related according to the thermochemical cycle of Eq. (2) and can be used to provide some information from the literature.

$$D(OM-O) + IE(MO) = D(OM^+-O) + IE(MO_2) \quad (2)$$

The review by Schröder et al. lists $D_0(OTa^+–O) = 6.07$ eV and $D_0(OW^+–O) = 5.72$ eV and cites the GIANT compilation. (Actually [30] contains no information about TaO_2^+, and the information in the GIANT compilation used to derive the WO_2^+ BDE indicates this value has an uncertainty of at least 1.17 eV, Table 1.) Heats of formation taken from the JANAF tables [33], which are based on Knudsen cell studies of Inghram et al. [37] provide D_0(OTa–O) as 6.61 ± 0.92 eV and this has also been measured as 6.87 ± 0.23 eV using the mass spectrometric Knudsen cell method [38]. The bond energy of 6.07 eV for $OTaO^+$ may have been obtained by combining the former neutral bond energy with IE(TaO) = 7.92 ± 0.1 eV [32] and $IE(TaO_2) = 8.5 \pm 0.5$ [38], indicating it should have an uncertainty of 1.05 eV, Table 1. Alternatively, we can combine IE(TaO) = 8.61 ± 0.02 eV [28] and $IE(TaO_2)$ values of 8.5 ± 0.5 [38] and 9 ± 0.5 eV [37] with the more precise $D_0(OTa–O) = 6.87 \pm 0.23$ eV to obtain $D(OTa^+–O)$ values of 6.98 ± 0.55 and 6.48 ± 0.55 eV, which we cite in Table 1 as 6.73 ± 0.80 eV given that neither $IE(TaO_2)$ value is precise. (Note that many of the literature IEs were determined solely to ascertain whether the species being probed were fragments or molecular species, hence their accuracy is questionable.) For WO_2, heats of formation given in the JANAF tables indicate the neutral OW–O bond energy is 6.15 ± 0.53 eV [33]. $IE(WO_2)$ has been reported as 9.6 ± 0.3 [39], 9.5 ± 0.5 [40], 9.9 ± 1.0 [41], 9.8 [42], and 9.9 ± 0.6 eV [36]. Along with IE(WO) = 8.1 ± 0.3 eV [34] and D(OW–O), these IEs can be combined to indicate that $D(OW^+–O)$ is anywhere between 3.4 and 5.4 eV, with the most precise $IE(WO_2)$ value suggesting $D(OW^+–O) = 4.6_5 \pm 0.7$ eV. Finally, there have been a few spectroscopic studies in which the ground state of TaO_2^+ has been identified as $^1A_1$ [43–45].

2. Experimental and computational section

2.1. General procedures

The guided ion beam tandem mass spectrometer on which these experiments were performed has been described in detail previously [46]. Briefly, MO^+ and MO_2^+ ions are generated in a direct current discharge flow tube (DC/FT) source described below [47], extracted from the source, accelerated, and focused into a magnetic sector momentum analyzer for mass selection of primary ions. The mass-selected ions are decelerated to a desired kinetic energy and focused into an octopole ion beam guide that uses radiofrequency electric fields to trap the ions in the radial direction and ensure complete collection of reactant and product ions [48,49]. The octopole passes through a static gas cell with an effective length of 8.26 cm that contains the reaction partner at a low pressure (usually less than ~0.3 mTorr) so that multiple ion–molecule collisions are improbable. All results reported here result from single bimolecular encounters, as verified by pressure dependence studies. The unreacted parent and product ions are confined radially in the guide until they drift to the end of the octopole where they are extracted, focused, and passed through a quadrupole mass filter for mass analysis of products. Ions are subsequently detected with a secondary electron scintillation ion detector [50] using standard pulse counting techniques. Reaction cross sections are calculated from product ion intensities relative to reactant ion intensities after correcting for background signals [51]. Uncertainties in absolute cross sections are estimated to be ±20%.

The kinetic energy of the ions is varied in the laboratory frame by scanning the dc bias on the octopole rods with respect to the potential of the ion source region. Laboratory (lab) ion energies are converted to energies in the center-of-mass frame (CM) by using the formula $E_{CM} = E_{lab}\, m/(m+M)$, where m and M are the neutral and ionic reactant masses, respectively. Two effects broaden the cross section data: the kinetic energy distribution of the reactant ion and the thermal motion of the neutral reactant gas (Doppler broadening) [52]. The absolute zero and the full width at half maximum (FWHM) of the kinetic energy distribution of the reactant ions are determined using the octopole beam guide as a retarding potential analyzer, as described previously [51]. The distributions of ion energies, which are independent of energy, are nearly Gaussian and have a typical FWHM of 0.45–0.64 eV (lab) in these studies. Uncertainties in the absolute zero of the energy scale are ±0.05 eV (lab).

2.2. Ion source

M^+ (M = Ta and W) ions are produced in a DC/FT source, consisting of a cathode held at a high negative voltage (1.3–2.0 kV) over which a flow of approximately 90% He and 10% Ar passes at a total pressure of 0.3–0.5 Torr. The dc-discharge ionizes Ar and then accelerates these ions into the cathode made of either tantalum or tungsten metal, thereby sputtering atomic metal cations. MO^+ and $MO_2{}^+$ ions are produced through the reaction of M^+ with N_2O by introducing the reactant gas 15 cm downstream of the discharge zone in the flow tube at a pressure of ~2 mTorr. These ions undergo ~10^5 thermalizing collisions with He and ~10^4 collisions with Ar along the flow tube before entering the guided ion beam apparatus. These collisions with the He/Ar flow gas stabilize and thermalize the ions both rotationally and vibrationally. In general, we assume that these ions are in their ground electronic state and that the internal energy of these molecular ions is well described by a Maxwell–Boltzmann distribution of rotational and vibrational states corresponding to 300 K, the temperature of the flow tube. Previous studies from this laboratory have shown that these assumptions are consistent with the production of thermalized molecular ions under similar conditions [53–57].

2.3. Data analysis

The cross sections of endothermic reactions are modeled using Eq. (3) [58–63]

$$\sigma(E) = \frac{\sigma_0 \Sigma g_i (E + E_i - E_0)^n}{E} \tag{3}$$

where σ_0 is an energy-independent scaling factor, E is the relative kinetic energy of the reactants, n is an adjustable parameter that characterizes the energy dependence of the process [61], and E_0 is the 0 K threshold for reaction of electronic, vibrational, and rotational state reactants. The model involves an explicit sum of the contributions of individual rovibrational states of the MO^+ and $MO_2{}^+$ reactant, denoted by i, having energies E_i and populations g_i. Before comparison with the experimental data, Eq. (3) is convoluted with the kinetic energy distributions of the reactant ions and neutral reactants at 300 K. The σ_0, n, and E_0 parameters are then optimized using a nonlinear least-squares analysis to give the best reproduction of the data [51]. Error limits for E_0 are calculated from the range of threshold values for different data sets over a range of acceptable n values combined with the absolute errors in the kinetic energy scale and internal energies of reactant ions.

2.4. Theoretical calculations

To establish the character of the molecular orbitals of the metal oxides and dioxides, quantum chemistry calculations were carried out with the B3LYP hybrid density functional method [64,65] and performed with the GAUSSIAN 09 suite of programs [66]. Ta and W are described using a basis set for Ta and W from Ohanessian et al. [67], which is based on the relativistic effective core potentials (ECP) of Hay–Wadt (HW) [68], equivalent to the Los Alamos ECP (LANL2DZ) basis set. Whereas the HW–ECP is optimized for neutral atoms, the altered basis set of Ohanessian et al. (HW+) accounts for differential contraction of the s orbitals compared to d orbitals induced by the positive charge. Calculations of thermochemistry and potential energy surfaces (relaxed potential energy surface scans) were conducted using a 6-311+G(3df) basis set for oxygen. We also examined results calculated using Def2TZVPP, a balanced basis set of triple zeta quality plus polarization for both elements [69], as well as the Stuttgart–Dresden (SDD) basis set [70] on the metal (retaining the 6-311+G(3df) basis on oxygen). The Def2TZVPP basis set includes f and g type polarization functions on Ta and W, whereas neither the HW+ nor SDD basis sets do. Both the Def2TZVPP and SDD basis set use ECPs developed by Andrae et al. for Ta and W [70]. In all cases, the thermochemistry calculated here is corrected for zero-point energies after scaling the vibrational frequencies by 0.9804 [71].

As a point of comparison, the calculated BDEs of O–O are 5.279 and 5.265 eV as calculated using the 6-311+G(3df) and Def2TZVPP basis sets compared to the experimental value of 5.115 eV [72]. In addition, the experimental ^3F excitation energy of Ta^+ (averaged over all spin–orbit levels) is 0.43 eV higher than the ^5F ground state (where the spin–orbit average is 0.47 eV above the ground level of $J = 1$) [73]. This experimental value can be compared to the excitation energies calculated at the B3LYP level using the HW+, SDD, and Def2TZVPP basis set of 0.40, 0.81, and 0.47 eV, respectively. For W^+, the experimental excitation energies of the ^6S and ^4F states are 0.41 and 1.07 eV, respectively, relative to the ^6D state (where the spin-orbit average lies 0.51 eV above the ground $J = 1/2$ level) [74]. The calculated B3LYP excitation energies with the HW+, SDD, and Def2TZVPP basis sets are 0.54, 0.44, and 0.51 eV for the ^6S excitation and 0.86, 0.88, and 0.82 eV for the ^4F excitation.

3. Experimental and theoretical results

3.1. CID of MO^+ with Xe

Cross sections for the interaction of TaO^+ and WO^+ with Xe were measured and are shown in Fig. 1. The products observed

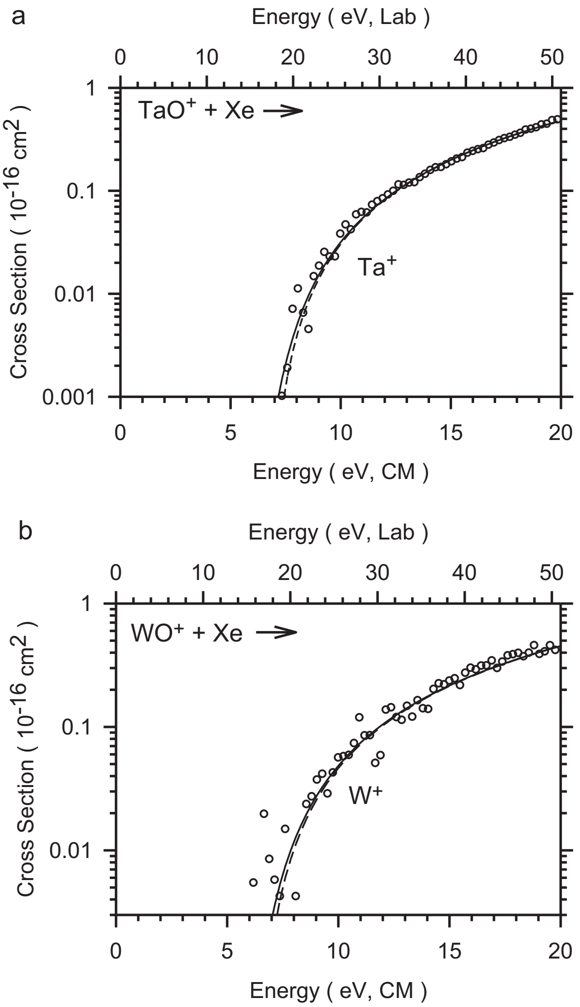

Fig. 1. Cross sections for collision-induced dissociation of TaO^+ (part a) and WO^+ (part b) with Xe as a function of kinetic energy in the center-of-mass frame (lower axis) and laboratory frame (upper axis). The best fits to the data (open circles) using Eq. (3) with parameters in Table 2 are shown as dashed lines. The solid lines show these models convoluted over the kinetic and internal energy distributions of the neutral reactant and ion.

correspond to reaction (4), a simple collision-induced dissociation process.

$$MO^+ + Xe \rightarrow M^+ + O + Xe \tag{4}$$

The cross section data for reaction (4) are analyzed using Eq. (3), and the fitting parameters obtained are listed in Table 2. The model reproduces the experimental data up to ~20 eV with thresholds of 7.01 ± 0.12 and 6.72 ± 0.10 eV for TaO^+ and WO^+, respectively. The threshold for CID can equal the M^+–O BDE as long as the interaction of M^+ with O is attractive everywhere, i.e., there are no barriers in excess of the asymptotic dissociation energy, and the dissociation produces ground state products. The former condition is almost certainly true here because the interaction of M^+ with O should be attractive at both long-range and short-range [58,60,75,76]. The latter condition is generally true when the dissociation pathway conserves spin, as it does here for the reactions $TaO^+(^3\Delta) \rightarrow Ta^+(^5F) + O(^3P)$ and $WO^+(^4\Sigma^-) \rightarrow W^+(^6D) + O(^3P)$. The CID thresholds of 7.01 ± 0.12 and 6.72 ± 0.10 eV for TaO^+ and WO^+ are in good agreement with the previously measured thermochemistry, Table 1. This may be somewhat serendipitous because CID experiments on strongly bound species with few internal degrees of freedom are sometimes found to measure only an upper limit to the thermodynamic BDE because of inefficiencies in the transfer of kinetic to internal energy in the collision process [14,57].

Table 2
Fitting parameters of Eq. (3) used to model reactions (4) and (5).

Reactant	Product	σ_0	n	E_0 (eV)
TaO^+	Ta^+	0.03 ± 0.01	2.3 ± 0.2	7.01 ± 0.12
WO^+	W^+	0.03 ± 0.01	2.4 ± 0.2	6.72 ± 0.10
TaO_2^+	TaO^+	0.91 ± 0.05	1.4 ± 0.1	6.08 ± 0.12
WO_2^+	WO^+	0.63 ± 0.13	1.5 ± 0.1	5.49 ± 0.09

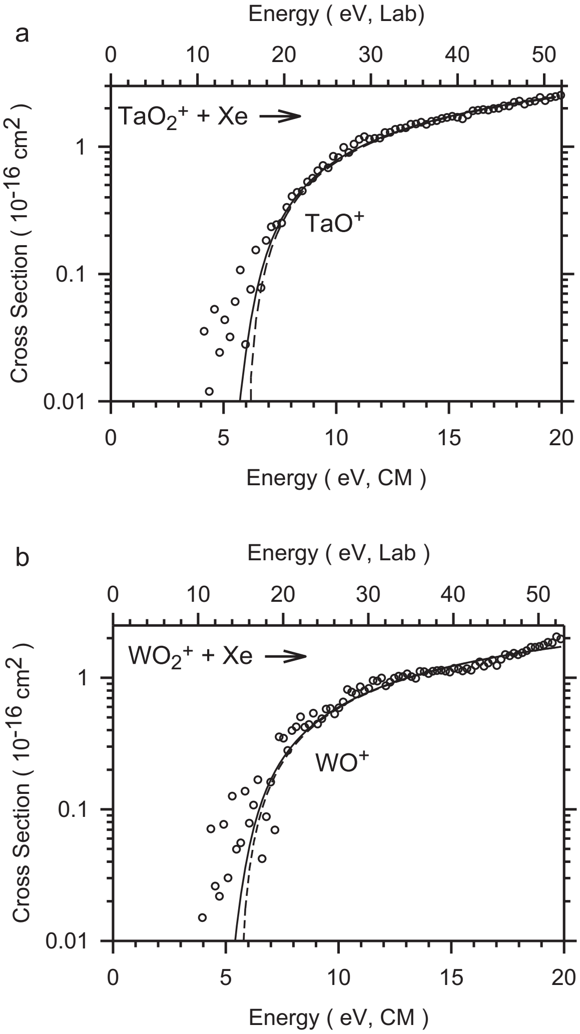

Fig. 2. Cross sections for collision-induced dissociation of $OTaO^+$ (part a) and OWO^+ (part b) with Xe as a function of kinetic energy in the center-of-mass frame (lower axis) and laboratory frame (upper axis). The best fits to the data (open circles) using Eq. (3) with parameters in Table 2 are shown as dashed lines. The solid lines show these models convoluted over the kinetic and internal energy distributions of the neutral reactant and ion.

3.2. CID of MO_2^+ with Xe

Cross sections for the interaction of Xe with TaO_2^+ and WO_2^+ are shown in Fig. 2. The products observed correspond to reaction (5).

$$MO_2^+ + Xe \rightarrow MO^+ + O + Xe \tag{5}$$

The cross section data for reaction (5) are analyzed using Eq. (3), and the fitting parameters obtained are listed in Table 2. For both processes, the model of Eq. (3) reproduces these cross sections well up to 20 eV. As for the monoxides, the threshold for CID can equal the OM^{+}–O BDE as long as there are no barriers in excess of the asymptotic dissociation energy and the dissociation produces ground state products, here $TaO^{+}(^{3}\Delta)$, $WO^{+}(^{4}\Sigma^{-})$, and $O(^{3}P)$, in spin allowed reactions. In both cases, the CID thresholds of 6.08 ± 0.12 and 5.49 ± 0.09 eV are in good agreement with the previous thermochemistry in Table 1, but are much more precise.

We also looked for but did not observe formation of M^{+} for either TaO_2^{+} or WO_2^{+}. This behavior contrasts with previous results for the CID of PtO_2^{+} with Xe [25], which produces both PtO^{+} and the bare Pt^{+} ion. An explanation for this was offered by Bohme and co workers [34] and relies on distinguishing between two cases according to whether the MO^{+} + O dissociation limit lies above or below the M^{+} + O_2 dissociation limit. When $D_0(MO^{+}) > D_0(O_2)$, the MO^{+} + O dissociation limit lies below the M^{+} + O_2 dissociation limit and exclusive loss of O is observed. When $D_0(MO^{+}) < D_0(O_2)$, the MO^{+} + O dissociation limit lies above the M^{+} + O_2 dissociation limit and loss of O_2 is observed, in competition with the entropically favored loss of O at higher energies. Ta and W fall into the former category, and Pt falls into the latter.

3.3. Reaction of MO^{+} with O_2

Cross sections for the reaction of MO^{+} with O_2 are shown in Fig. 3. The products observed correspond to the exothermic reaction (6).

$$MO^{+} + O_2 \rightarrow MO_2^{+} + O \tag{6}$$

The TaO_2^{+} and WO_2^{+} cross sections decrease with increasing kinetic energy, consistent with the behavior expected for barrierless exothermic ion-molecule reactions. This behavior can be described using the Langevin–Gioumousis–Stevenson (LGS) model [77], Eq. (7),

$$\sigma_{LGS} = \pi e\left(\frac{\alpha}{2\pi\varepsilon_0 E}\right)^{1/2} \tag{7}$$

where e is the charge on the electron, α is the polarizability volume of the neutral reactant molecule (1.57 Å^3 for O_2 [78]), and ε_0 is the permittivity of vacuum. As can be seen from Figure 3, the cross sections for both M = Ta and W have energy dependences of $E^{-0.5\pm0.1}$ at the lowest energies, as predicted by σ_{LGS}, with magnitudes approximately equivalent to σ_{LGS} in this energy range (within the 20% absolute uncertainty), indicating that the reactions occur with near unit efficiency. The reaction cross sections can also be converted into a room temperature rate constant using methods outlined previously [46,51]. For TaO^{+} and WO^{+}, this yields rate constants of (6.1 ± 1.2) and $(5.7 \pm 1.1) \times 10^{-10}$ cm^3 molecule^{-1} s^{-1}, respectively, compared to $k_{LGS} = 5.6 \times 10^{-10}$ cm^3 molecule^{-1} s^{-1}. These values compare favorably with the rate constants measured by Bohme and co-workers [34] in 0.35 Torr of helium at 295 K, (4.0 ± 1.2) and $(4.6 \pm 1.4) \times 10^{-10}$ cm^3 molecule^{-1} s^{-1}, respectively, corresponding to reaction efficiencies of 71 ± 21 and 82 ± 25%.

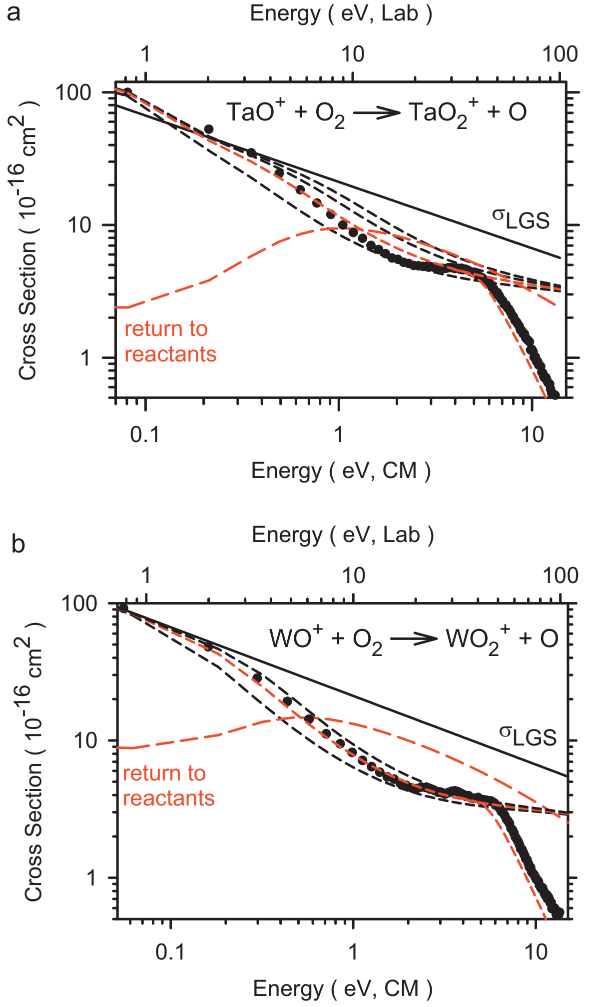

Fig. 3. Cross sections for reactions of TaO^{+} (part a) and WO^{+} (part b) with O_2 as a function of kinetic energy in the center-of-mass frame (lower *x*-axis) and laboratory frame (upper *x*-axis). The full line shows the theoretical collision cross section, σ_{LGS}. Dashed lines show the predictions of phase space theory for exothermicities of 0.4, 0.6 (in red), 0.8, and 1.0 eV (bottom to top) in part a and 0.3, 0.4 (in red), and 0.5 eV (bottom to top) in part b. (For interpretation of the references to color in this figure legend, the reader is referred to the web version of this article.) The cross section for the "return to reactants" is also shown for exothermicities of 0.6 and 0.4 in parts a and b, respectively.

Above about 0.3 eV, the cross sections begin to decrease more rapidly, approximately as $E^{-1.0\pm0.1}$. This effect can be attributed to angular momentum conservation constraints, as previously discussed in detail [56,79]. This argument recognizes that because the reduced mass of the products of reaction (6), μ', is smaller than that of the reactants, μ (μ'/μ is approximately 0.5 in these systems), the centrifugal barrier in the product channel can exceed that in the reactant channel for large angular momenta. This restricts the probability of reaction at higher kinetic energies, in essence by making it more favorable for the MO_3^{+} intermediate to dissociate back to reactants compared to going on to products. We have previously outlined a simple model to predict where these angular momentum constraints can restrict the product formation in exothermic reactions [56]. This begins at an energy given by Eq. (8),

$$E_c = \frac{(E - \Delta H)(\alpha' \mu'^2)}{(\alpha \mu^2)} \tag{8}$$

where α and α' are the polarizability volumes of the reactant and product neutrals (1.57 and 0.80 Å^3, respectively [78,80]), E is the relative kinetic energy of the reactants, and ΔH is the enthalpy of reaction. Using thermochemistry obtained above for TaO_2^{+} and WO_2^{+}, this model predicts that the TaO_2^{+} and WO_2^{+} cross sections will become constrained beginning at 0.17 ± 0.02 and 0.07 ± 0.02 eV, respectively, in reasonable agreement with the data.

A more precise way of examining this same phenomenon is to calculate the expected cross section using phase space theory (PST), performed using modified versions of programs originally developed by Chesnavich and Bowers [81]. These calculations assume that the potential interaction for the bimolecular reactants and products are ion-induced dipole attractions, i.e., the LGS cross section of Eq. (7) for the reactants, and then explicitly conserves both energy and angular momentum. The results for several assumed

Table 3
Theoretical results for MO^+ calculated at the B3LYP/HW+/6-311+G(3df) level.

Species	State	s(s + 1)[a]	Configuration	Energy (E_h)	Zero point energy (E_h)	E_{rel} (eV)	r(M–O) (Å)
O	^3P			−75.090915			
Ta^+	^5F	6.00	$6s^1 5d^3$	−57.362276		0.000	
	^3P	2.83[a]	$6s^2 5d^2$	−57.347516		0.402	
TaO^+	$^3\Delta$	2.01	$1\sigma^2 2\sigma^2 1\pi^4 3\sigma^1 1\delta^1$	−132.722996	0.002419	0.000	1.672
	$^1\Delta$	1.00[a]	$1\sigma^2 2\sigma^2 1\pi^4 3\sigma^1 1\delta^1$	−132.701893	0.002441	0.575	1.668
	$^1\Sigma^+$	0.00	$1\sigma^2 2\sigma^2 1\pi^4 3\sigma^2$	−132.693091	0.002493	0.816	1.665
	$^3\Sigma^-$	2.01	$1\sigma^2 2\sigma^2 1\pi^4 1\delta^2$	−132.691392	0.002342	0.858	1.679
	$^1\Sigma^-$	1.00[a]	$1\sigma^2 2\sigma^2 1\pi^4 1\delta^2$	−132.683503	0.002359	1.073	1.677
	$^5\Pi$	6.00	$1\sigma^2 2\sigma^2 1\pi^3 3\sigma^1 1\delta^2$	−132.595267	0.001723	3.457	1.881
	$^3\Pi$	2.78[a]	$1\sigma^2 2\sigma^2 1\pi^3 3\sigma^1 1\delta^2$	−132.583770	0.001748	3.770	1.873
	$^3\Phi$	2.01	$1\sigma^2 2\sigma^2 1\pi^3 3\sigma^2 1\delta^1$	−132.573944	0.001782	4.039	1.865
W^+	^6D	8.75	$6s^1 5d^4$	−67.345887		0.000	
	^6S	8.75	$6s^0 5d^5$	−67.326103		0.538	
	^4F	3.75	$6s^1 5d^4$	−67.314176		0.863	
WO^+	$^4\Sigma^-$	3.78	$1\sigma^2 2\sigma^2 1\pi^4 3\sigma^1 1\delta^2$	−142.693739	0.002479	0.000	1.648
	$^2\Gamma$	1.75[a]	$1\sigma^2 2\sigma^2 1\pi^4 3\sigma^1 1\delta^2$	−142.662911	0.002533	0.840	1.642
	$^2\Sigma^-$	1.75[a]	$1\sigma^2 2\sigma^2 1\pi^4 3\sigma^1 1\delta^2$	−142.651493	0.002537	1.151	1.642
	$^2\Delta$	0.76	$1\sigma^2 2\sigma^2 1\pi^4 3\sigma^2 1\delta^1$	−142.639796	0.002543	1.470	1.644
	$^4\Pi$	3.77	$1\sigma^2 2\sigma^2 1\pi^4 1\delta^2 2\pi^1$	−142.620987	0.002267	1.974	1.703

[a] State suffers from spin contamination.

exothermicities are shown in Fig. 3. In the case of Ta, the PST predicted cross sections capture the general energy behavior of the experimental cross section, with $\Delta H = -0.6$ eV yielding the best overall reproduction of the data. This is somewhat lower than the exothermicity of 0.96 ± 0.12 eV obtained from the CID measurements, however, an exothermicity this large does not agree with these data as well, as shown by the upper dashed curve in Fig. 3a. In the case of W, excellent agreement is observed between the experimental and the PST predicted cross sections, with $\Delta H = -0.4$ eV providing the best match. This is in agreement with the exothermicity of 0.38 ± 0.09 eV determined from the CID measurements. The additional curves shown in each part of the figure provide a rough estimate of the uncertainty in the ΔH value that could be obtained from the PST model, i.e., about ±0.2 eV for Ta and ±0.1 eV for W. These comparisons provide substantial confidence in the accuracy of the thermochemistry derived here for the MO_2^+ species.

At still higher energies, the MO_2^+ cross sections decline even more rapidly and now deviate strongly from the PST predictions. This is because dissociation of the MO_2^+ products to form $MO^+ + O$ can begin starting at $D_0(O_2) = 5.115$ eV. A simple model for such dissociations has previously been developed [82] and depends only on the energy onset for dissociation (set to 5.115 eV here) and a parameter p describing the energy dependence analogous to n in Eq. (3). This model for the subsequent dissociation probability ($p = 2$ for both metals) is multiplied by the best PST cross sections and shown in Fig. 3. It can be seen that the energy dependence of the data at high energy is reproduced nicely in both cases, although dissociation appears to be delayed somewhat. (Indeed, if the onsets are shifted to ~6 eV, the data are reproduced very well.) Such delays can occur if the initial reaction preferentially places energy in translation of the products instead of being distributed statistically.

3.4. Theoretical results: metal oxide cations

The bonding in diatomic transition metal oxides has been discussed by Schröder et al. [29]. The valence orbitals are 1σ (largely O 2s), 2σ (metal–oxygen sigma bonding), 1π (metal–oxygen pi bonding), 1δ (metal 5d nonbonding), 3σ (largely a metal 6s5d hybrid), 2π (metal–oxygen pi antibonding), and 4σ (metal–oxygen sigma antibonding). Configuration interaction between the 1σ and 2σ orbitals could drive the 2σ above the 1π, and the relative order of the 1δ and 3σ nonbonding orbitals is also unclear. For TaO^+, we calculate a $^3\Delta$ ($1\sigma^2 2\sigma^2 1\pi^4 3\sigma^1 1\delta^1$) ground state, Table 3, with the lowest lying excited state being the singlet-coupled version of this state, $^1\Delta$ having the same electron configuration and lying 0.58 eV above the ground state. Additional excited states, $^1\Sigma^+$, $^3\Sigma^-$, and $^1\Sigma^-$, have energies 0.82, 0.86, and 1.07 eV above the ground state, respectively. All five of these states have TaO triple bonds (occupied 2σ and 1π orbitals) with the remaining two electrons occupying the nonbonding 3σ and 1δ orbitals in different ways. Higher-lying excited states, Table 3, involve exciting an electron from the 1π bonding orbital and thus have excitation energies >3.4 eV above the ground state. All low-lying states have bond lengths of 1.66–1.68 Å, whereas the higher lying excited states have longer bonds (1.86–1.88 Å), indicative of a lower bond order. At a similar level of theory, B3LYP/LANL2DZ, Wu et al. [83] also found the TaO^+ ground state to be $^3\Delta$ and the $^1\Sigma^+$ excited state to be 0.87 eV higher in energy. It can also be noted that previous calculations have suggested a $^3\Sigma^-$ ground state at the BP86/LANL2DZ [45] level and a $^1\Sigma^+$ ground state at the B3LYP/LANL2DZ level [43].

The ground state of WO^+ is calculated to be $^4\Sigma^-$ ($1\sigma^2 2\sigma^2 1\pi^4 3\sigma^1 1\delta^2$), Table 3. Low-lying excited states include the low-spin coupled $^2\Gamma$, $^2\Sigma^-$, and $^2\Delta$ lying 0.84, 1.15, and 1.47 eV above the ground state, respectively. Both the ground state and low-lying excited states have bond lengths of 1.64–1.65 Å. We also located a $^4\Pi$ state having an excitation energy of 1.97 eV and a bond length of 1.70 Å, consistent with occupation of the antibonding 2π orbital. At a lower level of theory, B3LYP/HW/6-31G(d), Bohme and co-workers [34] found the $^4\Sigma^-$, $^2\Sigma^-$, and $^4\Pi$ states with excitation energies of 0.0, 0.8, and 2.0 eV, respectively, values that agree nicely with those calculated here.

The theoretical BDEs are compared with various experimental values, including the present CID thresholds, in Table 4. B3LYP calculations using the HW+ and SDD basis sets with calculated BDEs of 7.28 and 6.99 eV, respectively, give the best agreement compared to the experimental BDEs of 7.10 ± 0.12 eV [23] and our CID threshold of 7.01 ± 0.12 eV. Values calculated at the CCSD(T) level using any basis set were all higher, >7.48 eV, and values calculated at the BHLYP level are much too low, <6.54 eV. For WO^+, our previous WO^+ BDE of 6.77 ± 0.07 eV and our CID threshold of 6.72 ± 0.10 eV again agree well with values calculated at the B3LYP level with the HW+ and SDD basis sets. The CCSD(T) values using the Def2 and SDD basis sets also give reasonable agreement, whereas the BHLYP values are again too low.

In all of these comparisons, it should be realized that spin–orbit effects are not included in these theoretical values, i.e., the 0 K experimental BDEs correspond to dissociation to the lowest spin–orbit state of the metal cation, whereas the theoretical num-

Table 4
Theoretical and experimental bond dissociation energies in eV at 0 K.

Bond	Theory					Experiment	
	State	Basis set	B3LYP	BHLYP	CCSD(T)	CID threshold	Literature BDE[a]
TaO^+	$^3\Delta$	HW+	7.28	6.14	7.67	7.01 ± 0.12	7.10 ± 0.12
		Def2	7.61	6.54	7.56		7.18 ± 0.14
		SDD	6.99	5.84	7.48		8.15 ± 0.65
WO^+	$^4\Sigma^-$	HW+	6.92	5.68	6.07	6.72 ± 0.10	6.77 ± 0.07
		Def2	7.11	5.93	6.54		6.68 ± 0.53
		SDD	6.80	5.56	6.51		7.16 ± 0.43
							5.46 ± 0.43
TaO_2^+	$^1A_1$	HW+	5.79	4.77	6.24	6.08 ± 0.12	6.07 ± 1.05
		Def2	5.93	4.97	6.09		6.73 ± 0.80
		SDD	5.70	4.68	6.05		
WO_2^+	$^2A_1$	HW+	5.61	4.39	5.53	5.49 ± 0.09	5.72 ± 1.17
		Def2	5.80	4.66	5.35		4.6_5 ± 0.7
		SDD	5.56	4.34	5.26		

[a] Values from Table 1.

bers correlate with the average of all spin–orbit levels of the ground state of the metal ion, differences of 0.466 and 0.514 eV for Ta^+ and W^+, respectively. Corrections of the theoretical BDEs by subtracting these excitation energies ignores spin–orbit coupling in the metal oxide cations. For TaO, the spin–orbit splitting in the $^2\Delta$ ground state is 0.435 eV [33] and has been calculated to be as much as 0.56 eV for the related TaC^+ molecule [84]. Because the magnitudes of the spin–orbit coupling in the atomic ions and the molecular species are nearly the same (and the latter unknown for the specific product species considered here), no corrections for spin–orbit effects have been made.

3.5. Theoretical results: metal dioxide cations

A description of the bonding in transition metal dioxides has been detailed previously by Kretzschmar et al. [85] and can be qualitatively thought of in the following way, given that the molecule has C_{2v} symmetry along the z axis with the molecule lying in the xz plane. The $1a_1$ orbital is in-plane π-like bonding and is formed from the $5d_{x^2-z^2}$ orbital of the metal and the $2p_z$ of each oxygen atom. There are two sets of doubly occupied, σ-bonding orbitals ($1b_2$ and $2a_1$) resulting from interaction of the $5d_{xz}$ orbital with two $2p_x$ orbitals and the $5d_{y^2-z^2}$ orbital with the $2p_x$ orbitals of each oxygen atom along with some contributions of the metal 6s orbital. The $1a_2$ and $1b_1$ orbitals form a set of doubly occupied out-of-plane π-like orbitals, which involve the $2p_y$ orbitals on oxygen and the $5d_{xy}$ and $5d_{yz}$ orbitals on the metal. The $2b_2$ orbital, which is mostly nonbonding in character, is formed from the $2p_z$ orbitals of oxygen. The $3a_1$ orbital is a σ-like antibonding orbital, which is derived from the $5d_{y^2}$ along with 6s character and the two $2p_x$ orbitals on oxygen. Higher-lying orbitals include $3b_2$, $4a_1$, $2b_1$, and $2a_2$, which are the antibonding versions of the $1b_2$, $1a_1$, $1b_1$, and $1a_2$ bonding orbitals, and $5a_1$, mainly metal 6s.

For TaO_2^+, our B3LYP calculations find a $^1A_1$ ground state, in agreement with previous calculations [43,45,83] with a bond angle of 103.7°, Table 5. The $^1A_1$ ground state has an electron configuration of $(1a_1)^2(1b_2)^2(1b_1)^2(1a_2)^2(2a_1)^2(2b_2)^2$. The bonding in TaO_2^+ for each Ta–O bond involves 5 electrons in a bonding orbital and one electron in a nonbonding orbital to give a bond order of 2.5, which is reasonable given the strong BDE in this system. Excited states of TaO_2^+ include a $^3B_2$ state lying 1.49 eV above the ground state with additional excited states 2.77–6.91 eV above the ground state, Table 5. These states all involve excitations to antibonding orbitals such that their bond lengths are greater than that of the ground state. Several low-lying singlet excited states were located computationally but in all cases they were spin contaminated with an $s(s+1)$ value around 1.00, meaning these states contain extensive triplet character. In all cases, these singlet states had bond lengths, angles, and energies comparable to their triplet counterparts, and their energies varied with bond angle in an identical fashion to the corresponding triplet states.

For WO_2^+, the ground state is $^2A_1$ with a $(1a_1)^2(1b_2)^2(1b_1)^2(1a_2)^2(2a_1)^2(2b_2)^2(3a_1)^1$ configuration and a bond angle of 103.1°, Table 5. The bond order of WO_2^+ is similar to that of TaO_2^+, with the exception that the unpaired electron occupies an orbital with antibonding character making the bond

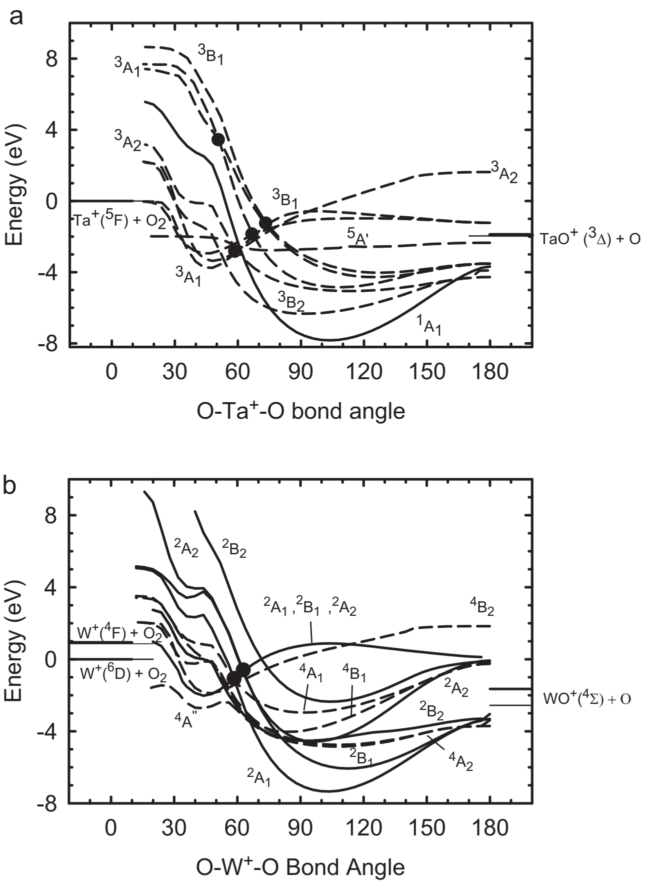

Fig. 4. Relaxed potential energy surface scans of the bond angle for the TaO_2^+ (part a) and WO_2^+ (part b) systems calculated at the B3LYP/HW+/6-311+G(3df) level. Solid and dashed lines represent singlet and triplet/quintet surfaces in part a and doublet and quartet surfaces in part b, respectively. Calculated energies of reactant and product asymptotes are indicated by horizontal bars to the left and right, respectively. Thicker horizontal bars indicate experimental energies of reactants and products. Large circles indicate avoided crossings.

Table 5
Bond lengths (Å), bond angles, and relative energies for MO_2^+ calculated at the B3LYP/HW+/6-311+G(3df) level.

Species	State	Configuration	s(s + 1)	r(M–O) (Å)	Angle (°)	E_{rel} (eV)
TaO_2^+	$^1A_1$	$(1a_1)^2(1b_2)^2(1b_1)^2(1a_2)^2(2a_1)^2(2b_2)^2$	0.00	1.700	103.7	0.00
	$^3B_2$	$(1a_1)^2(1b_2)^2(1b_1)^2(1a_2)^2(2a_1)^2(2b_2)^1(3a_1)^1$	2.03	1.753	92.7	1.49
	$^3A_2$	$(1a_1)^2(1b_2)^2(1b_1)^2(1a_2)^2(2a_1)^2(2b_2)^1(2b_1)^1$	2.03	1.775	113.5	2.77
	$^3A_1$	$(1a_1)^2(1b_2)^2(1b_1)^2(1a_2)^2(2a_1)^1(2b_2)^2(3a_1)^1$	2.02	1.743	109.2	2.91
	$^3A_1$	$(1a_1)^2(1b_2)^2(1b_1)^1(1a_2)^2(2a_1)^2(2b_2)^2(2b_1)^1$	2.05	1.811	124.9	3.55
	$^3B_1$	$(1a_1)^2(1b_2)^2(1b_1)^2(1a_2)^2(2a_1)^1(2b_2)^2(2b_1)^1$	2.03	1.790	127.6	3.72
	$^3A_1$	$(1a_1)^2(1b_2)^2(1b_1)^2(1a_2)^2(2a_1)^2(3a_1)^1(4a_1)^1$	2.03	1.866	46.1	4.04
	$^3A_2$	$(1a_1)^2(1b_2)^2(1b_1)^2(1a_2)^2(2a_1)^2(2a_2)^1(3a_1)^1$	2.00	1.867	48.1	4.46
	$^3B_1$	$(1a_1)^2(1b_2)^2(1b_1)^2(1a_2)^2(2a_1)^2(2b_1)^1(3a_1)^1$	2.02	1.877	45.9	4.87
	$^5A'$	$(1a')^2(1a'')^2(2a')^2(3a')^2(4a')^1(2a'')^1(5a')^1(3a'')^1$	6.01	1.715 2.157	75.3	5.06
	$^5A_2$	$(1a_1)^2(1b_2)^2(1b_1)^2(1a_2)^2(2a_1)^1(2b_2)^1(2b_1)^1(3a_1)^1$	6.01	1.894	138.4	5.26
	$^3A_2$	$(1a_1)^2(1b_2)^2(1b_1)^2(1a_2)^2(2a_1)^1(2b_2)^2(2a_2)^1$	2.03	1.779	97.5	5.48
	$^3B_2$	$(1a_1)^2(1b_2)^2(1b_1)^2(1a_2)^2(2a_1)^1(2b_2)^2(3b_2)^1$	2.01	1.831	119.8	6.91
WO_2^+	$^2A_1$	$(1a_1)^2(1b_2)^2(1b_1)^2(1a_2)^2(2a_1)^2(2b_2)^2(3a_1)^1$	0.76	1.676	103.1	0.00
	$^2B_1$	$(1a_1)^2(1b_2)^2(1b_1)^2(1a_2)^2(2a_1)^2(2b_2)^2(2b_1)^1$	0.75	1.692	112.4	1.27
	$^4A_2$	$(1a_1)^2(1b_2)^2(1b_1)^2(1a_2)^2(2a_1)^2(2b_2)^1(3a_1)^1(2b_1)^1$	3.79	1.745	108.7	2.51
	$^2A_2$	$(1a_1)^2(1b_2)^2(1b_1)^2(1a_2)^2(2a_1)^2(2b_2)^2(2a_2)^1$	0.77	1.714	96.7	2.77
	$^2B_2$	$(1a_1)^2(1b_2)^2(1b_1)^2(1a_2)^2(2a_1)^2(2b_2)^1(3a_1)^2$	0.82	1.723	92.8	2.82
	$^4B_1$	$(1a_1)^2(1b_2)^2(1b_1)^2(1a_2)^2(2a_1)^2(2b_2)^1(2a_2)^1(3a_1)^1$	3.80	1.761	84.2	3.31
	$^4A_1$	$(1a_1)^2(1b_2)^2(1b_1)^2(1a_2)^2(2a_1)^2(2b_2)^1(2b_1)^1(2a_2)^1$	3.80	1.789	91.9	4.32
	$^4A''$	$(1a')^2(1a'')^2(2a')^2(2a'')^2(3a')^2(3a'')^1(4a')^1(5a')^1$	4.03	1.907	42.3	4.62
	$(^4B_1)$	$(1a_1)^2(1b_2)^2(1b_1)^2(1a_2)^2(2a_1)^2(3a_1)^1(2b_1)^1(4a_1)^1$				
	$^2B_2$	$(1a_1)^2(1b_2)^2(1b_1)^2(1a_2)^2(2a_1)^2(2b_2)^2(3b_2)^1$	0.76	1.730	104.4	4.97
	$^2B_1$	$(1a_1)^2(1b_2)^2(1b_1)^2(1a_2)^2(2a_1)^2(2b_1)^1(3a_1)^2$	1.75[a]	1.876	44.2	5.13
	$^2A_1$	$(1a_1)^2(1b_2)^2(1b_1)^2(1a_2)^2(2a_1)^2(3a_1)^2(4a_1)^1$	0.76	1.834	46.7	5.23
	$^2A_2$	$(1a_1)^2(1b_2)^2(1b_1)^2(1a_2)^2(2a_1)^2(2a_2)^1(3a_1)^2$	1.69[a]	1.859	47.2	5.37
	$^4B_2$	$(1a_1)^2(1b_2)^2(1b_1)^2(1a_2)^2(2a_1)^2(2b_1)^1(2a_2)^1(3a_1)^1$	3.76	1.876	46.7	5.42
	$^2A_1$	$(1a_1)^2(1b_2)^2(1b_1)^2(1a_2)^2(2a_1)^2(2b_2)^2(3a_1)^1$	1.62[a]	2.132	38.3	9.66
	$^2B_1$	$(1a_1)^2(1b_2)^2(1b_1)^2(1a_2)^2(2a_1)^2(2b_2)^2(2b_1)^1$	1.59[a]	2.199	36.1	10.56
	$^2A_2$	$(1a_1)^2(1b_2)^2(1b_1)^2(1a_2)^2(2a_1)^2(2b_2)^2(2a_2)^1$	0.78	2.104	39.9	11.28

[a] State suffers from spin contamination.

order between 2 and 2.5. This clearly explains the lower observed BDE of WO_2^+ versus TaO_2^+, Table 4. A $^2B_1$ state lying 1.27 eV above the $^2A_1$ ground state was found with other states lying 2.51–11.28 eV higher in energy, Table 5. The lowest excitations involve moving the electron in the $3a_1$ antibonding orbital into other, more antibonding orbitals.

The calculated BDEs of TaO_2^+ compare favorably with the CID threshold of 6.08 ± 0.12 eV, Table 4. Particularly good agreement is found for the CCSD(T) values of 6.05–6.24 eV. The B3LYP values are also in fair agreement although somewhat lower, 5.70–5.93 eV. The BHLYP values are again much too low (by >1 eV). For WO_2^+, the CID threshold value of 5.49 ± 0.09 eV compares well with the B3LYP values, which range from 5.56–5.80 eV, and the CCSD(T) values of 5.26–5.53 eV. At the BHLYP level, the values again are consistently lower than the experimental value (by >0.8 eV). Overall, the agreement between experiment and theory is comparable to that observed for the metal monoxides, lending credence to the accuracy of the thermochemistry obtained here experimentally.

3.6. Potential energy surfaces for MO_2^+

Calculated potential energy surfaces for interaction of Ta^+ and W^+ with O_2 ($^3\Sigma^-$) are shown in Fig. 4. In most cases, species have C_{2v} symmetry throughout. Table 5 lists the geometries and energies of various stable states of the MO_2^+ species calculated at the B3LYP/HW+/6-311+G(3df) level of theory.

In the interaction of O_2 ($^3\Sigma_g^-$) with $Ta^+(^5F)$, Fig. 4a, the first step is formation of an association complex intermediate, the lowest of which is $Ta^+(O_2)$ ($^3A_1$), which has an energy 3.75 eV below the $Ta^+ + O_2$ asymptote. This intermediate has a bond angle of 46.1° and a configuration of $1a_1{}^2 1b_2{}^2 1b_1{}^2 1a_2{}^2 2a_1{}^2 3a_1{}^1 4a_1{}^1$. There are also $^3A_2$ and $^3B_1$ states of $Ta^+(O_2)$ that lie 0.4 and 0.8 eV higher in energy, respectively, and have similar bond lengths and angles. They differ in their electron configuration by the occupation of the $4a_1$, $2a_2$, or $2b_1$ antibonding orbitals, such that they are nearly degenerate. As the OTaO bond angle gets larger, the potential energy surfaces evolve into the more strongly bound tantalum dioxide cationic species. Here, the ground state of TaO_2^+ is $^1A_1$, which cannot be formed in a spin-allowed process from ground state $Ta^+(^5F) + O_2$ ($^3\Sigma_g^-$) and therefore can only be accessed by a curve crossing with triplet surfaces. The minimum on the $^1A_1$ surface lies 7.83 eV below the $Ta^+ + O_2$ asymptote. Above the $^1A_1$ surface lie the $^3B_2$, $^3A_2$, $^3A_1$, $^3A_1$, and $^3B_1$ surfaces (corresponding to the excited states discussed above) with minima lying 1.49, 2.77, 2.91, 3.55, and 3.72 eV above the $^1A_1$ minimum, respectively. There is also a $^5A'$ state that lies 2.77 eV below the $Ta^+(^5F) + O_2$ ($^3\Sigma_g^-$) asymptote (5.06 eV above the $^1A_1$ GS of TaO_2^+). This state has a minimum around 75°, is relatively flat from 60 to 180°, and correlates to the $TaO^+ + O$ asymptote at small angles because of the C_S symmetry. Importantly, all of the surfaces have minima that lie below the $TaO^+(^3\Delta) + O(^3P)$ product asymptote, 1.96 eV below the $Ta^+ + O_2$ asymptote (1.98 ± 0.12 eV experimentally).

For the activation of O_2 ($^3\Sigma_g^-$) by $W^+(^6D)$, the first step is the formation of an association complex intermediate, $W^+(O_2)$ ($^4A''$, nearly $^4B_1$), which lies 2.69 eV below the $W^+ + O_2$ asymptote. Seven other states of $W^+(O_2)$ were also located and lie 0.51–6.66 eV higher in energy, Table 5. As the bond angle of the $W^+(O_2)$ ($^4A''$) state increases, it crosses a surface having $^4A_2$ symmetry (which is avoided in C_S symmetry) that leads to a minimum 4.54 eV below the $W^+ + O_2$ asymptote. This species is the lowest quartet state of the WO_2^+ dioxide cation. A $^4B_1$ and $^4A_1$ state lie 0.80 and 1.81 eV higher in energy, whereas the $^2A_1$ ground state has an energy of −7.31 eV relative to the $W^+ + O_2$ asymptote. The $^2B_1$, $^2A_2$, and $^2B_2$ excited states discussed above lie 1.27, 2.77, and 2.82 eV above the $^2A_1$ state. The doublet states cannot be formed in spin-allowed processes from ground state $W^+(^6D)$ and O_2 ($^3\Sigma_g^-$) and therefore can only be accessed by a curve crossing with the quartet surfaces. All of the WO_2^+ states lie lower than the $WO^+(^4\Sigma^-) + O(^3P)$ product asymptote, 1.61 eV below the $W^+ + O_2$ asymptote (1.66 ± 0.07 eV experimentally).

In both metal systems, formation of ground state $MO^+ + O$ products can evolve in spin-allowed pathways from any of the MO_2^+ species, including the ground state. Clearly, these dissociation pathways require breaking C_{2v} symmetry. The observation that the thresholds for formation of MO^+ in the CID of MO_2^+ are consistent with the thermochemistry determined in the literature indicates that there are no barriers in excess of the endothermicity of the reaction, consistent with the qualitative character of the PESs shown in Fig. 4. These surfaces also are consistent with the observation that formation of MO^+ in the reaction of M^+ with O_2 is exothermic and barrierless (as observed experimentally [23]) and can proceed in a spin-allowed fashion by remaining on one of the triplet surfaces evolving from $Ta^+(^5F) + O_2\ (^3\Sigma_g^-)$ or quartet surfaces evolving from $W^+(^6D) + O_2\ (^3\Sigma_g^-)$.

Explicit calculations of MO_3^+ species were not pursued here, but one imagines that the reactions of TaO^+ and WO^+ with O_2 can proceed initially by formation of an associative complex $OTa^+(O_2)$ and $OW^+(O_2)$, with peroxide-like structures. Cleavage of the O_2 bond from such intermediates could lead to formation of $TaO_2^+(^1A_1) + O(^3P)$ and $WO_2^+(^2A_1) + O(^3P)$ products or covalently bound MO_3^+ species could be formed as well. These latter species cannot form double bonds to all oxygens as this formally places the metals in 7+ oxidation states, whereas the maximum oxidation state is 5+ for Ta and 6+ for W. Overall, the reactions $TaO^+(^3\Delta) + O_2(^3\Sigma_g^-) \rightarrow TaO_2(^1A_1) + O(^3P)$ and $WO^+(^4\Sigma^-) + O_2(^3\Sigma_g^-) \rightarrow WO_2(^2A_1) + O(^3P)$ are spin-allowed, consistent with their high efficiency, Fig. 3.

4. Summary

In this study, guided ion beam tandem mass spectrometry is used to generate TaO^+, WO^+, TaO_2^+, and WO_2^+ in a direct current discharge/flow tube (DC/FT) ion source. CID experiments of all four species with Xe are obtained with threshold energies reported in Tables 2 and 4. Reasonable agreement between these CID thresholds and literature thermochemistry is obtained for all systems. The thermochemistry for the metal dioxide cations also agrees that with obtained from the observations that reactions of both metal monoxide cations with O_2 are exothermic. Phase space theory calculations of the energetic behavior for these reactions are also in reasonable agreement with the exothermicities obtained from the CID reactions. Thus, the present results provide thermochemistry for TaO_2^+ and WO_2^+ that is considerably more precise than previous values, Table 1

Detailed quantum mechanical calculations are also performed for the metal monoxide and metal dioxide species. The nature of the bonding in the MO^+ and MO_2^+ species is analyzed at the B3LYP, BHLYP, and CCSD(T) levels of theory. Basis sets used for the metals include HW+, SDD, and Def2TZVPP, and for oxygen 6-311G(3df). Reasonable agreement between theory and the experimental results for the metal oxide and dioxide systems is found for most levels of theory, with BHLYP performing rather poorly. Potential energy surfaces for the interaction of the atomic metal cations with O_2 are also calculated at the B3LYP/HW+/6-311G(3df) level of theory. These surfaces demonstrate that dissociation of the MO_2^+ species can occur from the ground state by loss of an O atom, with no barriers in excess of endothermicity, consistent with the experimental results.

Acknowledgements

This work is supported by the National Science Foundation, CHE-1049580, the Chemical Sciences, Geosciences, and Biosciences Division, Office of Basic Energy Sciences, U. S. Department of Energy, and in part by the National Nuclear Security Administration, Office of Nonproliferation Research and Development (NA-22).

References

[1] D. Smith, N.G. Adams, Plasma Chemistry I, Vol. 89 of Topics in Current Chemistry, Springer-Verlag, Berlin, 1980, p. 1.

[2] E. Murad, J. Geophys. Res 83 (1978) 5525, Tech. Rep. AFGL-TR-77-0235, Air Force Geophysics Laboratory, Hanscom Air Force Base, MA, 1977.

[3] R.A. Sheldon, in: D.H. Barton, A.E. Martell, D.T. Sawyer (Eds.), The Activation of Dioxygen and Homogeneous Catalytic Oxidation, Plenum, New York, 1993, p. 9;
R.A. Sheldon, J.K. Kochi, Metal-Catalyzed Oxidations of Organic Compounds, Academic, New York, 1981.

[4] N. Aristov, P.B. Armentrout, J. Phys. Chem. 90 (1986) 5135.

[5] S.K. Loh, E.R. Fisher, L. Lian, R.H. Schultz, P.B. Armentrout, J. Phys. Chem. 93 (1989) 3159.

[6] S.K. Loh, L. Lian, P.B. Armentrout, J. Chem. Phys. 91 (1989) 6148.

[7] E.R. Fisher, J.L. Elkind, D.E. Clemmer, R. Georgiadis, S.K. Loh, N. Aristov, L.S. Sunderlin, P.B. Armentrout, J. Chem. Phys. 93 (1990) 2676.

[8] D.E. Clemmer, J.L. Elkind, N. Aristov, P.B. Armentrout, J. Chem. Phys. 95 (1991) 3387.

[9] D.E. Clemmer, N.F. Dalleska, P.B. Armentrout, J. Chem. Phys. 95 (1992) 7263.

[10] D.E. Clemmer, N.F. Dalleska, P.B. Armentrout, Chem. Phys. Lett. 190 (1992) 259.

[11] M.R. Sievers, P.B. Armentrout, J. Chem. Phys. 102 (1995) 754.

[12] M.T. Rodgers, B. Walker, P.B. Armentrout, Int. J. Mass Spectrom. 182–183 (1999) 99.

[13] Y.-M. Chen, P.B. Armentrout, J. Chem. Phys. 103 (1995) 618.

[14] M.R. Sievers, Y.-M. Chen, P.B. Armentrout, J. Chem. Phys. 105 (1996) 6322.

[15] M.R. Sievers, P.B. Armentrout, Int. J. Mass. Spectrom. 103 (1998) 179.

[16] M.R. Sievers, P.B. Armentrout, J. Phys. Chem. A 102 (1998) 10754.

[17] M.R. Sievers, P.B. Armentrout, Inorg. Chem. 38 (1999) 397.

[18] M.R. Sievers, P.B. Armentrout, Int. J. Mass Spectrom. 185–187 (1999) 117.

[19] M.E. Weber, J.L. Elkind, P.B. Armentrout, J. Chem. Phys. 84 (1986) 1521.

[20] D.E. Clemmer, M.E. Weber, P.B. Armentrout, J. Chem. Phys. 96 (1992) 10888.

[21] N.F. Dalleska, P.B. Armentrout, Int. J. Mass Spectrom. Ion Process. 134 (1994) 203.

[22] X.-G. Zhang, P.B. Armentrout, J. Phys. Chem. A 107 (2003) 8904.

[23] C.S. Hinton, F.-X. Li, P.B. Armentrout, Int. J. Mass Spectrom. 280 (2009) 226.

[24] F.-X. Li, K. Gorham, P.B. Armentrout, J. Phys. Chem. A 114 (2010) 11043.

[25] X.-G. Zhang, P.B. Armentrout, J. Phys. Chem. A 107 (2003) 8915.

[26] B. Simard, P. Kowalczyk, A.M. James, Phys. Rev. 50 (1994) 846.

[27] J.B. Pedley, E.M. Marshall, J. Phys. Chem. Ref. Data 12 (1983) 967.

[28] J.M. Dyke, A.M. Ellis, M. Feher, A. Morris, A.J. Paul, J.C.H. Stevens, J. Chem. Soc., Faraday Trans. 2 (83) (1987) 1555.

[29] D. Schröder, H. Schwarz, S. Shaik, Struct. Bond 97 (2000) 91.

[30] S.G. Lias, J.E. Bartmess, J.F. Liebman, J.L. Holmes, R.D. Levin, W.G. Mallard, J. Phys. Chem. Ref. Data 17 (Suppl. 1) (1988) 1.

[31] E.G. Rauh, R.J. Ackermann, J. Chem. Phys. 70 (1979) 1004.

[32] R.J. Ackermann, E.G. Rauh, R.J. Thorn, J. Chem. Phys. 65 (1976) 1027.

[33] M.W. Chase, C.A. Davies, J.R. Downey, D.J. Frurip, R.A. McDonald, A.N. Syverud, JANAF thermodynamic tables, J. Phys. Chem. Ref. Data 14 (Suppl. 1) (1985) 1.

[34] V. Blagojevic, G.K. Koyanagi, V.V. Lavrov, G. Orlova, D.K. Bohme, Chem. Phys. Lett. 389 (2004) 303.

[35] M.D. Campbell-Miller, B. Simard, J. Opt. Soc. Am. B 13 (1996) 2115.

[36] G. Demaria, R.P. Burns, J. Drowart, M.G. Inghram, J. Chem. Phys. 32 (1960) 1373.

[37] M.G. Inghram, W.A. Chupka, J. Berkowitz, J. Chem. Phys. 27 (1957) 569.

[38] S. Smoes, J. Drowart, C.E. Myers, J. Chem. Thermodyn. 8 (1976) 225.

[39] A.V. Gusarov, I.S. Gotkis, L.N. Gorokhov, High Temp. 13 (1975) 324.

[40] G. Balducci, G. Gigli, M. Guido, J. Chem. Soc., Faraday Trans. 2 (77) (1981) 1107.

[41] R. Yamdagni, C. Pupp, R.F. Porter, J. Inorg. Nucl. Chem. 32 (1970) 3509.

[42] J. Drowart, G. Exsteen, G. Verhaegen, J. Chem. Soc., Faraday Trans. 60 (1964) 1920.

[43] M. Chen, X. Wang, L. Zhang, M. Yu, Q. Qin, Chem. Phys. 242 (1999) 81.

[44] X. Wang, Z. Gu, Q. Qin, Int. J. Mass Spectrom. 188 (1999) 205.

[45] M. Zhou, L. Andrews, J. Phys. Chem. A 102 (1998) 8251.

[46] S.K. Loh, D.A. Hales, L. Lian, P.B. Armentrout, J. Chem. Phys. 90 (1989) 5466.

[47] R.H. Schultz, P.B. Armentrout, Int. J. Mass Spectrom. Ion Process. 107 (1991) 29.

[48] E. Teloy, D. Gerlich, Chem. Phys. 4 (1974) 417.

[49] D. Gerlich, Adv. Chem. Phys. 82 (1992) 1.

[50] N.R. Daly, Rev. Sci. Instrum. 31 (1960) 264.

[51] K.M. Ervin, P.B. Armentrout, J. Chem. Phys. 83 (1985) 166.

[52] P.J. Chantry, J. Chem. Phys. 55 (1971) 2746.

[53] P.B. Armentrout, in: J.M. Brown, P. Hoffman (Eds.), Topics in Organometallic Chemistry, vol. 4-I, Springer-Verlag, Berlin, 1999, p. 1.

[54] I. Kretzschmar, D. Schröder, H. Schwarz, P.B. Armentrout, Adv. Metal Semicond. Clusters 5 (2001) 347.

[55] X.-G. Zhang, P.B. Armentrout, Organometallics 20 (2001) 4266.

[56] J.D. Burley, K.M. Ervin, P.B. Armentrout, Int. J. Mass Spectrom. Ion Process. 80 (1987) 153.

[57] X.-G. Zhang, R. Liyanage, P.B. Armentrout, J. Am. Chem. Soc. 123 (2001) 5563.

[58] P.B. Armentrout, Int. J. Mass Spectrom. 200 (2000) 219.

[59] W.J. Chesnavich, M.T. Bowers, J. Phys. Chem. 83 (1979) 900.

[60] P.B. Armentrout, Adv. Gas-Phase Ion Chem. 1 (1992) 83.
[61] F. Muntean, P.B. Armentrout, J. Chem. Phys. 115 (2001) 1213.
[62] N. Aristov, P.B. Armentrout, J. Am. Chem. Soc. 108 (1986) 1806.
[63] P.B. Armentrout, in: N.G. Adams, L.M. Babcock (Eds.), Advances in Gas Phase Metal Ion Chemistry, 1, JAI, Greenwich, 1992, p. 83.
[64] A.D. Becke, J. Chem. Phys. 98 (1993) 5648.
[65] C. Lee, W. Yang, R.G. Parr, Phys. Rev. B 37 (1988) 785.
[66] M.J. Frisch, G.W. Trucks, H.B. Schlegel, G.E. Scuseria, M.A. Robb, J.R. Cheeseman, G. Scalmani, V. Barone, B. Mennucci, G.A. Petersson, H. Nakatsuji, M. Caricato, X. Li, H.P. Hratchian, A.F. Izmaylov, J. Bloino, G. Zheng, J.L. Sonnenberg, M. Hada, M. Ehara, K. Toyota, R. Fukuda, J. Hasegawa, M. Ishida, T. Nakajima, Y. Honda, O. Kitao, H. Nakai, T. Vreven, J...A. Montgomery Jr., J.E. Peralta, F. Ogliaro, M. Bearpark, J.J. Heyd, E. Brothers, K.N. Kudin, V.N. Staroverov, R. Kobayashi, J. Normand, K. Raghavachari, A. Rendell, J.C. Burant, S.S. Iyengar, J. Tomasi, M. Cossi, N. Rega, J.M. Millam, M. Klene, J.E. Knox, J.B. Cross, V. Bakken, C. Adamo, J. Jaramillo, R. Gomperts, R.E. Stratmann, O. Yazyev, A.J. Austin, R. Cammi, C. Pomelli, J.W. Ochterski, R.L. Martin, K. Morokuma, V.G. Zakrzewski, G.A. Voth, P. Salvador, J.J. Dannenberg, S. Dapprich, A.D. Daniels, Ö. Farkas, J.B. Foresman, J.V. Ortiz, J. Cioslowski, D.J. Fox, Gaussian 09, Revision A.1, Gaussian, Inc., Wallingford, CT, 2009.
[67] G. Ohanessian, M.J. Brusich, W.A. Goddard III, J. Am. Chem. Soc. 112 (1990) 7179.
[68] P.J. Hay, W.R. Wadt, J. Chem. Phys. 82 (1985) 299.
[69] F. Weigend, R. Ahlrichs, Phys. Chem. Chem. Phys. 7 (2005) 3297.
[70] D. Andrae, U. Haeussermann, M. Dolg, H. Stoll, H. Preuss, Theor. Chem. Acta 77 (1990) 123.
[71] J.B. Foresman, A.E. Frisch, Exploring Chemistry with Electronic Structure Methods, Gaussian, Inc., Pittsburgh, PA, 1996.
[72] K.P. Huber, G. Herzberg, Molecular Spectra and Molecular Structure. IV. Constants of Diatomic Molecules, Van Nostrand Reinhold, New York, 1979.
[73] C.C. Kiess, J. Res. Natl. Bur. Stand. (U.S.) 66A (1962) 111.
[74] J.O. Ekberg, R. Kling, W. Mende, Phys. Scr. 61 (2000) 146.
[75] P.B. Armentrout, B.L. Kickel, in: B.S. Freiser (Ed.), Organometallic Ion Chemistry, Klewer, Dordrecht, 1996, p. 1.
[76] P.B. Armentrout, J. Simons, J. Am. Chem. Soc. 114 (1992) 8627.
[77] G. Gioumousis, D.P. Stevenson, J. Phys. Chem. 29 (1958) 294.
[78] E.W. Rothe, R.B. Bernstein, J. Chem. Phys. 31 (1959) 1619.
[79] N. Aristov, P.B. Armentrout, J. Phys. Chem. 91 (1987) 6178.
[80] T.M. Miller, B. Bederson, Adv. Atom. Mol. Phys. 13 (1977) 1.
[81] W.J. Chesnavich, M.T. Bowers, J. Chem. Phys. 68 (1978) 901.
[82] M.E. Weber, J.L. Elkind, P.B. Armentrout, J. Chem. Phys. 84 (1986) 1521.
[83] Z.J. Wu, Y. Kawazoe, J. Meng, J. Mol. Struct. Theochem. 764 (2006) 123.
[84] D. Majumdar, K. Balasubramanian, Chem. Phys. Lett. 294 (1998) 273.
[85] I. Kretzschmar, A. Fiedler, J.N. Harvey, D. Schröder, H. Schwarz, J. Phys. Chem. A 101 (1997) 6252.